

Rashba Spin-Orbit Coupling Enhanced Carrier Lifetime in Organometal Halide Perovskites

Fan Zheng, Liang Z. Tan, Shi Liu, and Andrew M. Rappe*

*The Makineni Theoretical Laboratories, Department of Chemistry, University of Pennsylvania,
Philadelphia, Pennsylvania 19104-6323, USA*

E-mail: rappe@upenn.sas.edu

*To whom correspondence should be addressed

Abstract

Organometal halide perovskites are promising solar-cell materials for next-generation photovoltaic applications. The long carrier lifetime and diffusion length of these materials make them very attractive for use in light absorbers and carrier transporters. While these aspects of organometal halide perovskites have attracted the most attention, the consequences of the Rashba effect, driven by strong spin-orbit coupling, on the photovoltaic properties of these materials are largely unexplored. In this work, taking the electronic structure of methylammonium lead iodide as an example, we propose an intrinsic mechanism for enhanced carrier lifetime in 3D Rashba materials. Based on first-principles calculations and a Rashba spin-orbit model, we demonstrate that the recombination rate is reduced due to the spin-forbidden transition. These results are important for understanding the fundamental physics of organometal halide perovskites and for optimizing and designing the materials with better performance. The proposed mechanism including spin degrees of freedom offers a new paradigm of using 3D Rashba materials for photovoltaic applications.

The organometal halide perovskites (OMHPs) have attracted significant attention due to the rapid increase in their photovoltaic power conversion efficiency. In the past 2 years, the reported efficiency of OMHP-based solar cells has almost doubled from 9.7%¹ to over 20%,²⁻⁴ making OMHPs very promising for low-cost and high-efficiency photovoltaics. Methylammonium lead iodide, $\text{CH}_3\text{NH}_3\text{PbI}_3$ (MAPbI₃), and other closely-related hybrid perovskites such as Cl-doped and Br-doped MAPbI₃ (MAPbI_{3-x}Cl_x and MAPbI_{3-x}Br_x), $(\text{NH}_2)_2\text{CHPbI}_3$ (formamidinium lead iodide, FAPbI₃), and Sn-doped MAPbI₃ (MAPb_xSn_{1-x}I₃), all display band gaps (1.1 to 2.1 eV) in the visible light region, favorable for photovoltaic applications.⁵⁻¹³ The class of materials also possesses strong light absorption, fast charge generation and high carrier mobility.^{14,15} In particular, exceptionally long carrier lifetime and diffusion length have been observed in MAPbI₃ and MAPbI_{3-x}Cl_x, making them better solar cell candidates than other semiconductors with similar band gaps and absorption coefficients.¹⁶⁻¹⁸

Intense research has been directed toward understanding and further enhancing the long carrier lifetime and diffusion length in OMHPs. Previous studies reported a relatively low defect

concentration in MAPbI₃,^{19–23} which reduces the scattering centers for nonradiative charge carrier recombination. Recently, it has been suggested that the spatial carrier segregation caused by disorder-induced localization²⁴ or domains acting as internal *p-n* junctions^{25–27} may reduce the recombination rate. Though many of the OMHPs are 3D Rashba materials driven by strong spin-orbit coupling (SOC) and bulk ferroelectricity,^{28–31} the effects of spin and orbital degrees of freedom on photovoltaic applications are largely unexplored beyond band gap engineering.²⁹ In this work, we focus on an intrinsic mechanism for the enhancement of long carrier lifetime due to the Rashba splitting. Using first-principles calculations and effective models, we find that the Rashba splitting arising from SOC under inversion symmetry breaking can result in spin-allowed and spin-forbidden recombination channels. The spin-forbidden recombination path has a significantly slower transition rate due to the mismatch of spin and momentum. The spin-allowed recombination path, though kinetically favorable, can be suppressed under appropriate spin texture due to the low population of free carriers. Taking the electronic structures of MAPbI₃ under various distortions as examples, we show that the proposed mechanism is possible under room temperature, and is potentially responsible for the long carrier lifetime in OMHPs. This spin-dependent recombination mechanism highlights the possibility of using 3D Rashba materials for efficient photovoltaic applications.

Fig. 1 illustrates the mechanism for enhancing the carrier lifetime in a generic 3D Rashba material. The strong spin-orbit coupling effect from heavy elements (e.g., Pb, Sn, I and Br) and the polar distortion (e.g., aligned molecular dipoles in OMHPs) give rise to the Rashba effect, which lifts the two-fold degeneracy of bands near the band gap. Near the band gap, the spin degeneracies of the conduction and valence bands are lifted, giving rise to “inner” and “outer” bands with opposite spin textures, characterizing spin rotation direction as “clockwise” ($\chi = -1$) and “counterclockwise” ($\chi = +1$) (Fig. 1). The photo excitation process creates free electrons and holes, which can quickly relax to band extrema in the presence of inelastic phonon scattering. When the spin textures of conduction band minimum (CBM) and valence band maximum (VBM) are opposite, the radiative recombination of $C_{\chi=-1} \rightarrow V_{\chi=+1}$ is a spin-forbidden transition due

to the mismatch of spin states. This prevents rapid recombination as the photon-induced spin-flip is a slow process.³² Moreover, the minimum of the $C_{\chi=-1}$ band is slightly shifted compared to the maximum of the $V_{\chi=+1}$ band (momentum mismatch). This creates an indirect band gap for recombination, which further slows down the recombination process due to the requirement of a phonon with the right momentum.³³ In the following, we use the terms favorable and unfavorable relative spin helicity to describe cases when the VBM and CBM have opposite and aligned spins, respectively.

The spin texture and carrier population of the CBM and VBM play key roles in enhancing carrier lifetime. Our first-principles density functional theory (DFT) calculations support the realization of this mechanism in OMHPs. Taking the pseudocubic phase MAPbI₃ as an example, we explore the carrier dynamics after the photoexcitation. Using Fermi's golden rule, we calculate the inelastic phonon scattering rate (see Methods). As shown in Fig. 2, the relaxation rate ($\approx 10^{15}\text{s}^{-1}$) increases as a function of carrier energy with sharp jumps corresponding to thresholds for optical phonon emission. We find that the organic molecule plays an important role for carrier relaxation. The modes that are most important for carrier relaxation are MA translation, CH/NH twisting, and CH/NH stretching, and they contribute equally to the relaxation of both electrons and holes.

Our calculations reveal that the phonon-induced carrier relaxation rate value is many orders of magnitude faster than the electron-hole recombination rate ($\approx 10^9\text{ s}^{-1}$).^{34,35} Therefore, the carriers will rapidly thermalize and form a quasi-static equilibrium distribution near the CBM and VBM. In the ideal case of low temperatures and large Rashba splitting, nearly all free carriers are located at the band extrema, and the effects of spin and momentum mismatch on the enhancement of the carrier lifetime will be the greatest. This effect is less strong at finite temperatures and small Rashba splitting because of the thermal occupation of $C_{\chi=1}$ and $V_{\chi=-1}$ bands, which opens spin-allowed recombination paths such as $C_{\chi=-1} \rightarrow V_{\chi=-1}$. In the case of favorable relative spin helicity, we investigate this temperature effect by examining the Rashba splitting using a Rashba Hamiltonian:³⁶

$$H_R = \frac{\hbar^2 k^2}{2m} + \hbar v_R \hat{z} \times \vec{k} \cdot \vec{\sigma} \quad (1)$$

$$E_{k,s} = \frac{\hbar^2 (k_z^2 + k_\perp^2)}{2m} + s \hbar v_R k_\perp, \quad k_\perp = \sqrt{k_x^2 + k_y^2} \quad (2)$$

For the parameters m and v_R representing the band mass and Rashba interaction respectively, we use values obtained from the DFT band structure of fully-relaxed MAPbI₃. We find that the conduction band Rashba splitting (0.108 eV) is much larger than the thermal energy scale, while the valence band Rashba splitting (0.016 eV) is comparable to the thermal energy scale. Since electronic correlations are not fully captured in DFT,¹³ these values are likely lower bounds of the true splitting. These relatively large Rashba splittings are likely to give rise to a significant enhancement in carrier lifetime even at room temperature.

There is an additional factor, arising from the unique features of Rashba band structure, which promotes occupation of the band extrema. In contrast to the band extrema of ordinary parabolic bands in semiconductors which are points in momentum space, those of Rashba materials are one-dimensional rings (Fig. 1). This leads to an increase in the density of states at low energies, resulting in a population of carriers heavily skewed towards the band extrema (Fig. 3a and b) and consequently reduces the overall recombination rate due to the reasons of spin and momentum mismatch as discussed above.

The magnitude of Rashba splitting depends on the amount of polar distortion and the strength of the SOC, both of which can be captured by the Rashba velocity parameter v_R . We calculate the averaged recombination rate

$$\langle \tau^{-1} \rangle = \sum_{\chi, \chi'} \frac{\int d^3k \tau_{\chi, \chi'}^{-1}(k) n_\chi^e(k) n_{\chi'}^h(k)}{\int d^3k n_\chi^e(k) n_{\chi'}^h(k)} \quad (3)$$

where $\tau_{\chi, \chi'}^{-1}(k) = B_{\chi, \chi'} n_\chi^e(k) n_{\chi'}^h(k)$ is the band- and momentum-resolved recombination rate. The spin-mismatch effect is captured by the rate constant $B_{\chi, \chi'}$, which is larger when χ and χ' have parallel spins than otherwise. Enhancement of density of states enters via the temperature depen-

dent electron and hole occupation numbers $n^e(k)$ and $n^h(k)$, which tend to peak at different k points because of momentum mismatch. In order to quantify the effect of Rashba splitting on the recombination rate, we define the unitless lifetime enhancement factor as the ratio $\langle \tau^{-1} \rangle_{v_R=0} / \langle \tau^{-1} \rangle_{v_R}$, where $\langle \tau^{-1} \rangle_{v_R}$ is the average lifetime when SOC is taken into account, and $\langle \tau^{-1} \rangle_{v_R=0}$ refers to a calculation where SOC is explicitly set to zero in the Rashba model (Fig. 3c). Upon tuning the Rashba splitting continuously in our model, we find that the lifetime enhancement factor increases approximately exponentially with Rashba splitting - a consequence of the exponential behavior of carrier occupation numbers near the tail of the Fermi-Dirac distribution. Our model predicts that a Rashba splitting of 0.1 eV can give rise to an order of magnitude enhancement of carrier lifetime.

As we have seen, the presence lifetime enhancement is enabled by the relative spin helicity of VBM and CBM, while the amount of enhancement depends on the magnitude of the Rashba splitting. The symmetry-breaking distortions that influence relative spin helicity and splitting magnitude are therefore intimately related to the SOC enhancement of carrier lifetime. To reveal the relation, we start with a tight binding model of the inorganic PbI_3^- lattice (see Methods). The displacements of Pb atoms along the z direction give rise to effective hoppings between Pb s - and p -orbitals along the equatorial direction (Fig. 4a), which would vanish by symmetry in the absence of such displacements. Similarly, displacement of the apical I atoms along the z direction changes Pb-I bond lengths and effective hoppings along the apical direction (Fig. 4b). These modifications of hopping parameters create the effective inversion symmetry breaking electric fields described by $\hbar v_R$ in our low-energy theory model (Eq. 1). In this model, we find that the spin textures of the valence bands and conduction bands depend on the combination of Pb and I displacements. By shifting Pb and I atoms, we can control the spin textures of the valence and conduction bands, creating favorable and unfavorable relative spin helicities. As we now proceed to show, this picture is confirmed with DFT calculations.

We focus on two phases of MAPbI_3 , pseudocubic phase (α phase) and tetragonal phase (β phase).¹¹ The pseudocubic phase of MAPbI_3 has space group $P4mm$ with $a = b = 6.31$ and $c = 6.32$, which can only hold ferroelectric distortions, such as displacements of Pb and apical I atoms.

Shown in Fig. 4d are the DFT-calculated spin textures and averaged Rashba splittings at VBM and CBM respectively for a given pair of Pb and I displacements (see Methods). The areas outlined by the solid red lines indicate the structures with favorable relative spin helicities, which also have relatively large band splittings. We find that these structures have Pb and apical I displaced along opposite directions. This is consistent with typical ferroelectric distortions in inorganic ferroelectrics such as BaTiO₃ and PbTiO₃. It is noted that large apical I displacement tends to drive the system away from the region with favorable relative spin helicity to unfavorable spin helicity (Fig. 4d).

We further explore the relationship between relative spin helicity and local distortions in tetragonal MAPbI₃,¹¹ which is observed at room temperature. The space group of the tetragonal phase is identified as *I4cm*, allowing both ferroelectric distortion and PbI₆ octahedral rotation (Fig. 4e). Fig. 4f shows the spin textures and the averaged Rashba splitting for different Pb and I displacements in *I4cm* space group. The tetragonal phase exhibits similar displacement-helicity relationship to the cubic phase, indicating that the Rashba splitting can also enhance the carrier lifetime in tetragonal phase.

At room temperature, switchable, large (≈ 100 nm) ferroelectric domains have recently been observed experimentally in MAPbI₃.³⁷ Various theoretical studies also suggested the existence of local polar regions at room temperature.^{24,26,38} The structures that are energetically accessible at room temperature are highlighted by dashed red lines in Fig. 4d and f, which cover a large region displaying favorable spin textures. Hence, our proposed mechanism is likely to be realized in MAPbI₃ at room temperature, and provides a possible explanation of long carrier lifetime. Moreover, recent studies of carrier dynamics under magnetic field also illustrate the significance of spin in carrier recombinations.³⁹⁻⁴¹

Rashba SOC enhanced carrier lifetime highlights the potential of 3D Rashba materials for photovoltaic applications. The ability to incorporate different organic molecules in OMHPs provides a robust avenue to design 3D Rashba materials. By tuning the dipole magnitude of organic molecules in halide perovskites, the spin helicities and band splittings can be manipulated via the

Pb and I displacements as discussed above. Conventional experimental techniques of controlling bulk polarization (e.g, epitaxial strain) can also be applied to optimize power conversion efficiency.

In summary, we have proposed an intrinsic mechanism for enhancing carrier lifetime in 3D Rashba materials. In the case of OMHPs, such mechanism can be realized by the joint action of molecules (electron-phonon coupling) and PbI_3 sublattices (giving rise to spin-orbit coupling). The photoexcited carriers quickly relax to band edges due to the electron-phonon coupling. When the spin textures for CBM and VBM are opposite, the Rashba splitting of bands close to the band gap results in spin-allowed and spin-forbidden recombination paths. The spin-forbidden recombination path has slow transition rate due to mismatch of spin and momentum. The spin-allowed recombination path, though kinetically favorable, will only influence a smaller amount of carriers. In order to achieve this favorable spin helicity, we explore different Pb and I displacement giving rise to different spin textures. A tight binding model is developed to explain this spin-displacement relation. This mechanism allows OMHPs to behave like direct-gap semiconductors upon photoexcitation, and like indirect-gap semiconductors during radiative recombination, simultaneously harnessing the large carrier densities of the former and the long lifetimes of the latter. Our work is the first to introduce this mechanism and highlights the importance of Rashba effect and structural distortion for achieving long carrier lifetime and consequently long diffusion length in organometal halide perovskites.

Methods

DFT and Electron-phonon coupling The plane-wave DFT package QUANTUM-ESPRESSO⁴² with the Perdew-Burke-Ernzerhof⁴³ functional is used to perform electronic structure and electron-phonon coupling calculation. Norm-conserving, designed nonlocal pseudopotentials were generated with the OPIUM package.^{44,45} We calculate the inelastic phonon scattering rate for electrons and holes using Fermi's golden rule:^{35,46}

$$\tau_{k,n \rightarrow n'}^{(ph)-1} = \hbar^{-1} \frac{V}{(2\pi)^3} \sum_{\mathbf{v}} \int d^3k' |g_{\mathbf{v},k,k'}^{n,n'}|^2 \delta(E_{k,n} - E_{k',n'} - \hbar\omega_{\mathbf{v}}) \quad (4)$$

where k and n are the wavevector and band index respectively, ν denotes the phonon mode, $E_{k,n}$ are electronic band energies and V is the volume of the unit cell. The phonon frequencies ω_ν and electron-phonon matrix elements $g_{\nu,k,k'}^{n,n'}$ are obtained from density functional perturbation theory (DFPT).⁴⁷

Lifetime enhancement factor The rate constant $B_{\chi,\chi'}$ in Eq. 3 of spin-allowed ($\chi = \chi' = \pm 1$) and spin-forbidden ($\chi \neq \chi'$) transitions are obtained from averaged DFT calculated oscillation strength. For example, $B_{1,1} \approx 3.7B_{1,-1}$.

Tight-binding model The tight-binding model is based on PbI_3^- structure. Pb $6s$, Pb $6p$ and the I $5p$ orbitals are included in this model with spin degree of freedom. The tight-binding Hamiltonian is:

$$H_{\text{TB}} = H_{\text{hop}} + H_{\text{SOC}} \quad (5)$$

where H_{hop} considers the nearest neighbor hopping between two orbitals, described by t_{sp} , $t_{pp\sigma}$ and $t_{pp\pi}$ for s - p σ hopping, p - p σ hopping and p - p π hopping respectively. H_{SOC} is the on-site SOC term defined as $\lambda_{\text{Rashba}} \mathbf{L} \cdot \mathbf{S}$. Hopping parameters and λ_{Rashba} are fitted to DFT band structures of pseudocubic MAPbI_3 with experimental lattice constants. We reduce our tight-binding Hamiltonian into the Rashba effective model (Eq. 1) in two steps, following the procedure outlined in.²⁸ First, the I p orbitals are removed by projecting H_{TB} to the subspace of Pb orbitals:

$$H_{\text{Pb}} = \mathcal{P}H_{\text{TB}}\mathcal{P} + \mathcal{P}H_{\text{TB}}\mathcal{Q}\frac{1}{E - \mathcal{Q}H_{\text{TB}}\mathcal{Q}}\mathcal{Q}H_{\text{TB}}\mathcal{P} \quad (6)$$

where \mathcal{P} and \mathcal{Q} are projection operators to the Pb and I subspaces respectively. This results in an effective Hamiltonian H_{Pb} containing inversion symmetry breaking terms which modify the effective hopping between Pb orbitals.²⁸ Next, H_{Pb} is reduced to H_R using a similar projection to the CBM and VBM.

Rashba splitting energy phase diagram The Rashba splitting energy is defined as $|\Delta E^R| = \min [\langle E_{C,s=\text{CBM}+1} - E_{C,s=\text{CBM}} \rangle, \langle E_{V,s=\text{VBM}} - E_{V,s=\text{VBM}-1} \rangle]$. Here, the sign of ΔE^R is indicated as +1 for favorable spin helicity, and -1 for unfavorable spin helicity. “ $\langle \rangle$ ” indicates the average

over k points near CBM or VBM.

References

- (1) Kim, H.-S.; Lee, C.-R.; Im, J.-H.; Lee, K.-B.; Moehl, T.; Marchioro, A.; Moon, S.-J.; Humphry-Baker, R.; Yum, J.-H.; Moser, J. E. et al. Lead iodide perovskite sensitized all-solid-state submicron thin film mesoscopic solar cell with efficiency exceeding 9%. *Sci. Rep.* **2012**, *2*, 591.
- (2) Zhou, H.; Chen, Q.; Li, G.; Luo, S.; Song, T.-b.; Duan, H.-S.; Hong, Z.; You, J.; Liu, Y.; Yang, Y. Interface engineering of highly efficient perovskite solar cells. *Science* **2014**, *345*, 542–546.
- (3) Jeon, N. J.; Lee, H. G.; Kim, Y. C.; Seo, J.; Noh, J. H.; Lee, J.; Seok, S. I. o-Methoxy Substituents in Spiro-OMeTAD for Efficient Inorganic-Organic Hybrid Perovskite Solar Cells. *J. Am. Chem. Soc.* **2014**, *136*, 7837–7840.
- (4) NREL. Research Cell Efficiency Records. http://www.nrel.gov/ncpv/images/efficiency_chart.jpg.
- (5) Papavassiliou, G. C.; Koutselas, I. Structural, optical and related properties of some natural three-and lower-dimensional semiconductor systems. *Synth. Met.* **1995**, *71*, 1713–1714.
- (6) Noel, N. K.; Stranks, S. D.; Abate, A.; Wehrenfennig, C.; Guarnera, S.; Haghighirad, A.; Sadhanala, A.; Eperon, G. E.; Pathak, S. K.; Johnston, M. B. et al. Lead-Free Organic-Inorganic Tin Halide Perovskites for Photovoltaic Applications. *Energy Environ. Sci.* **2014**, *7*, 3061–3068.
- (7) Umari, P.; Mosconi, E.; De Angelis, F. Relativistic GW calculations on $\text{CH}_3\text{NH}_3\text{PbI}_3$ and $\text{CH}_3\text{NH}_3\text{SnI}_3$ perovskites for solar cell applications. *Sci. Rep.* **2014**, *4*, 4467–1–7.
- (8) Chiarella, F.; Zappettini, A.; Licci, F.; Borriello, I.; Cantele, G.; Ninno, D.; Cassinese, A.; Vaglio, R. Combined experimental and theoretical investigation of optical, structural, and

- electronic properties of $\text{CH}_3\text{NH}_3\text{SnX}_3$ thin films ($X = \text{Cl}, \text{Br}$). *Phys. Rev. B* **2008**, *77*, 045129.
- (9) Ogomi, Y.; Morita, A.; Tsukamoto, S.; Saitho, T.; Fujikawa, N.; Shen, Q.; Toyoda, T.; Yoshino, K.; Pandey, S. S.; Ma, T. et al. $\text{CH}_3\text{NH}_3\text{Sn}_x\text{Pb}_{(1-x)}\text{I}_3$ Perovskite Solar Cells Covering up to 1060 nm. *J. Phys. Chem. Lett.* **2014**, *5*, 1004–1011.
- (10) Eperon, G. E.; Stranks, S. D.; Menelaou, C.; Johnston, M. B.; Herz, L. M.; Snaith, H. J. Formamidinium lead trihalide: a broadly tunable perovskite for efficient planar heterojunction solar cells. *Energy Environ. Sci.* **2014**, *7*, 982–988.
- (11) Stoumpos, C. C.; Malliakas, C. D.; Kanatzidis, M. G. Semiconducting tin and lead iodide perovskites with organic cations: phase transitions, high mobilities, and near-infrared photoluminescent properties. *Inorg. Chem.* **2013**, *52*, 9019–9038.
- (12) Mosconi, E.; Quarti, C.; Ivanovska, T.; Ruani, G.; De Angelis, F. Structural and Electronic Properties of Organo-Halide Lead Perovskites: A Combined IR-Spectroscopy and Ab Initio Molecular Dynamics Investigation. *Phys. Chem. Chem. Phys.* **2014**, *16*, 16137–16144.
- (13) Filip, M. R.; Giustino, F. *GW* quasiparticle band gap of the hybrid organic-inorganic perovskite $\text{CH}_3\text{NH}_3\text{PbI}_3$: Effect of spin-orbit interaction, semicore electrons, and self-consistency. *Phys. Rev. B* **2014**, *90*, 245145.
- (14) Ponseca, J., Carlito S.; Savenije, T. J.; Abdellah, M.; Zheng, K.; Yartsev, A.; Pascher, T.; Harlang, T.; Chabera, P.; Pullerits, T.; Stepanov, A. et al. Organometal Halide Perovskite Solar Cell Materials Rationalized: Ultrafast Charge Generation, High and Microsecond-Long Balanced Mobilities, and Slow Recombination. *J. Am. Chem. Soc.* **2014**, *136*, 5189–5192.
- (15) Edri, E.; Kirmayer, S.; Mukhopadhyay, S.; Gartsman, K.; Hodes, G.; Cahen, D. Elucidating the charge carrier separation and working mechanism of $\text{CH}_3\text{NH}_3\text{PbI}_{3-x}\text{Cl}_x$ perovskite solar cells. *Nat. Commun.* **2014**, *5*, 3461.

- (16) Xing, G.; Mathews, N.; Sun, S.; Lim, S. S.; Lam, Y. M.; Graetzel, M.; Mhaisalkar, S.; Sum, T. C. Long-Range Balanced Electron- and Hole-Transport Lengths in Organic-Inorganic $\text{CH}_3\text{NH}_3\text{PbI}_3$. *Science* **2013**, *342*, 344–347.
- (17) Stranks, S. D.; Eperon, G. E.; Grancini, G.; Menelaou, C.; Alcocer, M. J.; Leijtens, T.; Herz, L. M.; Petrozza, A.; Snaith, H. J. Electron-hole diffusion lengths exceeding 1 micrometer in an organometal trihalide perovskite absorber. *Science* **2013**, *342*, 341–344.
- (18) Wehrenfennig, C.; Eperon, G. E.; Johnston, M. B.; Snaith, H. J.; Herz, L. M. High Charge Carrier Mobilities and Lifetimes in Organolead Trihalide Perovskites. *Adv. Mater.* **2014**, *26*, 1584–1589.
- (19) Kim, J.; Lee, S.-H.; Lee, J. H.; Hong, K.-H. The Role of Intrinsic Defects in Methylammonium Lead Iodide Perovskite. *J. Phys. Chem. Lett.* **2014**, *5*, 1312–1317.
- (20) Yin, W.-J.; Shi, T.; Yan, Y. Unusual defect physics in $\text{CH}_3\text{NH}_3\text{PbI}_3$ perovskite solar cell absorber. *Appl. Phys. Lett.* **2014**, *104*, 063903.
- (21) Du, M. H. Efficient carrier transport in halide perovskites: theoretical perspectives. *J. Mater. Chem. A* **2014**, *2*, 9091–9098.
- (22) Yamada, Y.; Endo, M.; Wakamiya, A.; Kanemitsu, Y. Spontaneous Defect Annihilation in $\text{CH}_3\text{NH}_3\text{PbI}_3$ Thin Films at Room Temperature Revealed by Time-Resolved Photoluminescence Spectroscopy. *J. Phys. Chem. Lett.* **2015**, *6*, 482–486.
- (23) Buin, A.; Pietsch, P.; Xu, J.; Voznyy, O.; Ip, A. H.; Comin, R.; Sargent, E. H. Materials Processing Routes to Trap-Free Halide Perovskites. *Nano Lett.* **2014**, *14*, 6281–6286.
- (24) Ma, J.; Wang, L.-W. Nanoscale charge localization induced by random orientations of organic molecules in hybrid perovskite $\text{CH}_3\text{NH}_3\text{PbI}_3$. *Nano Lett.* **2015**, *15*, 248–253.
- (25) Frost, J. M.; Butler, K. T.; Walsh, A. Molecular Ferroelectric Contributions to Anomalous Hysteresis in Hybrid Perovskite Solar Cells. *APL Mater.* **2014**, *2*, 081506.

- (26) Frost, J. M.; Butler, K. T.; Brivio, F.; Hendon, C. H.; van Schilfgaarde, M.; Walsh, A. Atomistic origins of high-performance in hybrid halide perovskite solar cells. *Nano Lett.* **2014**, *14*, 2584–2590.
- (27) Liu, S.; Zheng, F.; Koocher, N. Z.; Takenaka, H.; Wang, F.; Rappe, A. M. Ferroelectric Domain Wall Induced Band-Gap Reduction and Charge Separation in Organometal Halide Perovskites. *J. Phys. Chem. Lett.* **2015**, *6*, 693–699.
- (28) Kim, M.; Im, J.; Freeman, A. J.; Ihm, J.; Jin, H. Switchable $S = 1/2$ and $J = 1/2$ Rashba bands in ferroelectric halide perovskites. *Proc. Natl. Acad. Sci.* **2014**, *111*, 6900–6904.
- (29) Even, J.; Pedesseau, L.; Jancu, J.-M.; Katan, C. Importance of spin–orbit coupling in hybrid organic/Inorganic perovskites for photovoltaic applications. *J. Phys. Chem. Lett.* **2013**, *4*, 2999–3005.
- (30) Stroppa, A.; Di Sante, D.; Barone, P.; Bokdam, M.; Kresse, G.; Franchini, C.; Whangbo, M.-H.; Picozzi, S. Tunable ferroelectric polarization and its interplay with spin–orbit coupling in tin iodide perovskites. *Nat. Commun.* **2014**, *5*, 5900.
- (31) Amat, A.; Mosconi, E.; Ronca, E.; Quarti, C.; Umari, P.; Nazeeruddin, M. K.; Graetzel, M.; De Angelis, F. Cation-Induced Band-Gap Tuning in Organohalide Perovskites: Interplay of Spin-Orbit Coupling and Octahedra Tilting. *Nano Letters* **2014**, *14*, 3608–3616.
- (32) Liu, S.; Srinivasan, S.; Tao, J.; Grady, M. C.; Soroush, M.; Rappe, A. M. Modeling Spin-Forbidden Monomer Self-Initiation Reactions in Spontaneous Free-Radical Polymerization of Acrylates and Methacrylates. *J. Phys. Chem. A* **2014**, *118*, 9310–9318.
- (33) Motta, C.; Mellouhi, F. E.; Kais, S.; Tabet, N.; Alharbi, F.; Sanvito, S. Revealing the role of organic cations in hybrid halide perovskite $\text{CH}_3\text{NH}_3\text{PbI}_3$. *Nat. Commun.* **2015**, *6*, 7026.
- (34) Filippetti, A.; Delugas, P.; Mattoni, A. Radiative Recombination and Photoconversion of

- Methylammonium Lead Iodide Perovskite by First Principles: Properties of an Inorganic Semiconductor within a Hybrid Body. *J. Phys. Chem. C* **2014**, *118*, 24843–24853.
- (35) Kawai, H.; Giorgi, G.; Marini, A.; Yamashita, K. The Mechanism of Slow Hot-Hole Cooling in Lead-Iodide Perovskite: First-Principles Calculation on Carrier Lifetime from Electron–Phonon Interaction. *Nano Lett.* **2015**, ASAP.
- (36) Bychkov, Y. A.; Rashba, E. Properties of A 2D Electron Gas with Lifted Spectral Degeneracy. *JETP Lett.* **1984**, *39*, 78–81.
- (37) Kutes, Y.; Ye, L.; Zhou, Y.; Pang, S.; Huey, B. D.; Padture, N. P. Direct observation of ferroelectric domains in solution-processed $\text{CH}_3\text{NH}_3\text{PbI}_3$ perovskite thin films. *J. Phys. Chem. Lett.* **2014**, *5*, 3335–3339.
- (38) Quarti, C.; Mosconi, E.; De Angelis, F. Interplay of orientational order and electronic structure in methylammonium lead iodide: implications for solar cell operation. *Chem. Mater.* **2014**, 6557–6569.
- (39) Giovanni, D.; Ma, H.; Chua, J.; Grätzel, M.; Ramesh, R.; Mhaisalkar, S.; Mathews, N.; Sum, T. C. Highly Spin-Polarized Carrier Dynamics and Ultralarge Photoinduced Magnetization in $\text{CH}_3\text{NH}_3\text{PbI}_3$ Perovskite Thin Films. *Nano Lett.* **2015**, *15*, 1553–1558.
- (40) Hsiao, Y.-C.; Wu, T.; Li, M.; Hu, B. Magneto-Optical Studies on Spin-Dependent Charge Recombination and Dissociation in Perovskite Solar Cells. *Adv. Mater.* **2015**, ASAP.
- (41) Zhang, C.; Sun, D.; Sheng, C.-X.; Zhai, Y. X.; Mielczarek, K.; Vardeny, Z. V. Magnetic field effects in hybrid perovskite devices. *Nature Phys.* **2015**, ASAP.
- (42) Giannozzi, P.; Baroni, S.; Bonini, N.; Calandra, M.; Car, R.; Cavazzoni, C.; Ceresoli, D.; Chiarotti, G. L.; Cococcioni, M.; Dabo, I. et al. Quantum ESPRESSO: A modular and open-source software project for quantum simulations of materials. *J. Phys.: Condens. Matter* **2009**, *21*, 395502–20.

- (43) Perdew, J. P.; Burke, K.; Ernzerhof, M. Generalized Gradient Approximation Made Simple. *Phys. Rev. Lett.* **1996**, *77*, 3865–8.
- (44) Rappe, A. M.; Rabe, K. M.; Kaxiras, E.; Joannopoulos, J. D. Optimized Pseudopotentials. *Phys. Rev. B Rapid Comm.* **1990**, *41*, 1227–30.
- (45) Ramer, N. J.; Rappe, A. M. Designed Nonlocal Pseudopotentials for Enhanced Transferability. *Phys. Rev. B* **1999**, *59*, 12471–8.
- (46) Bernardi, M.; Vigil-Fowler, D.; Lischner, J.; Neaton, J. B.; Louie, S. G. Ab Initio Study of Hot Carriers in The First Picosecond after Sunlight Absorption in Silicon. *Phys. Rev. Lett.* **2014**, *112*, 257402.
- (47) Baroni, S.; de Gironcoli, S.; Dal Corso, A. Phonons and Related Crystal Properties from Density-Functional Perturbation Theory. *Rev. Mod. Phys.* **2001**, *73*, 515–562.

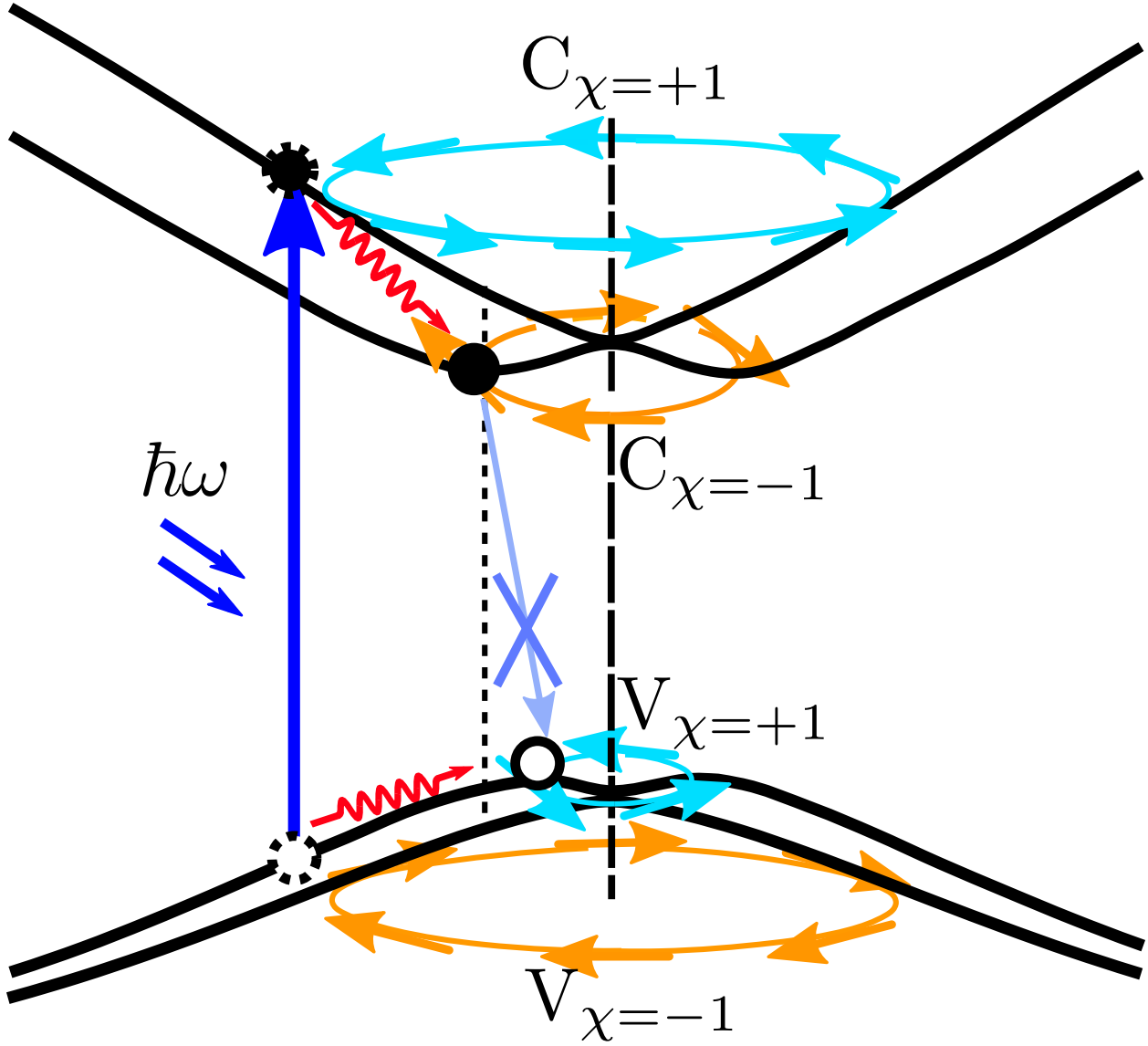


Figure 1: Diagram of Rashba bands and the electron transport path. The cyan and orange arrows indicate the directions of the spins. The spin texture χ indicates spin vortex direction, with its signs characterizing spin rotation in "clockwise" ($\chi = -1$) and "counterclockwise" ($\chi = +1$). After absorbing the photons, the excited electrons on conduction bands $C_{\chi=+1}$ and $C_{\chi=-1}$ will quickly relax to $C_{\chi=-1}$ band minimum due to the inelastic phonon scattering. Similarly, the holes will quickly relax to the $V_{\chi=+1}$ band maximum. However, the radiative recombination of $C_{\chi=-1} \rightarrow V_{\chi=+1}$ is a spin-forbidden process due to the opposite spin states they have. Moreover, the minimum of $C_{\chi=-1}$ band and the maximum of $V_{\chi=+1}$ band are located in different positions in the Brillouin Zone. This creates an indirect band gap for recombination, which further slows down the recombination process.

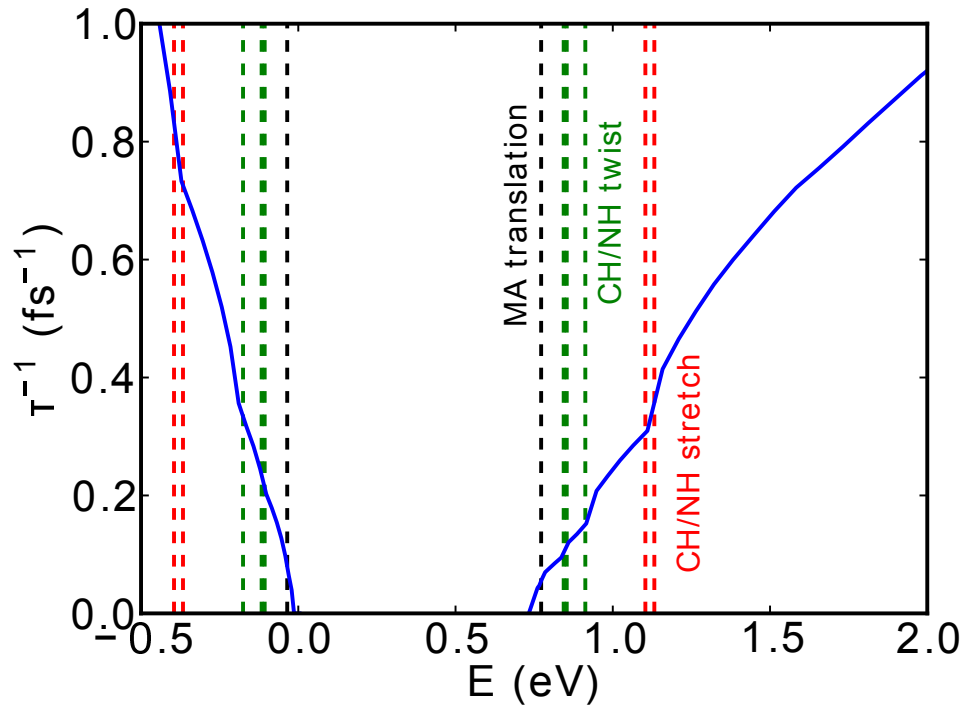


Figure 2: Dependence of phonon-induced relaxation rate on carrier energies (blue lines) for electrons (positive energies) and holes (negative energies). The VBM is located at $E = 0$ eV, and the CBM is located at $E = 0.73$ eV. The energies of phonon modes that contribute strongly to carrier relaxation are shown as dotted lines.

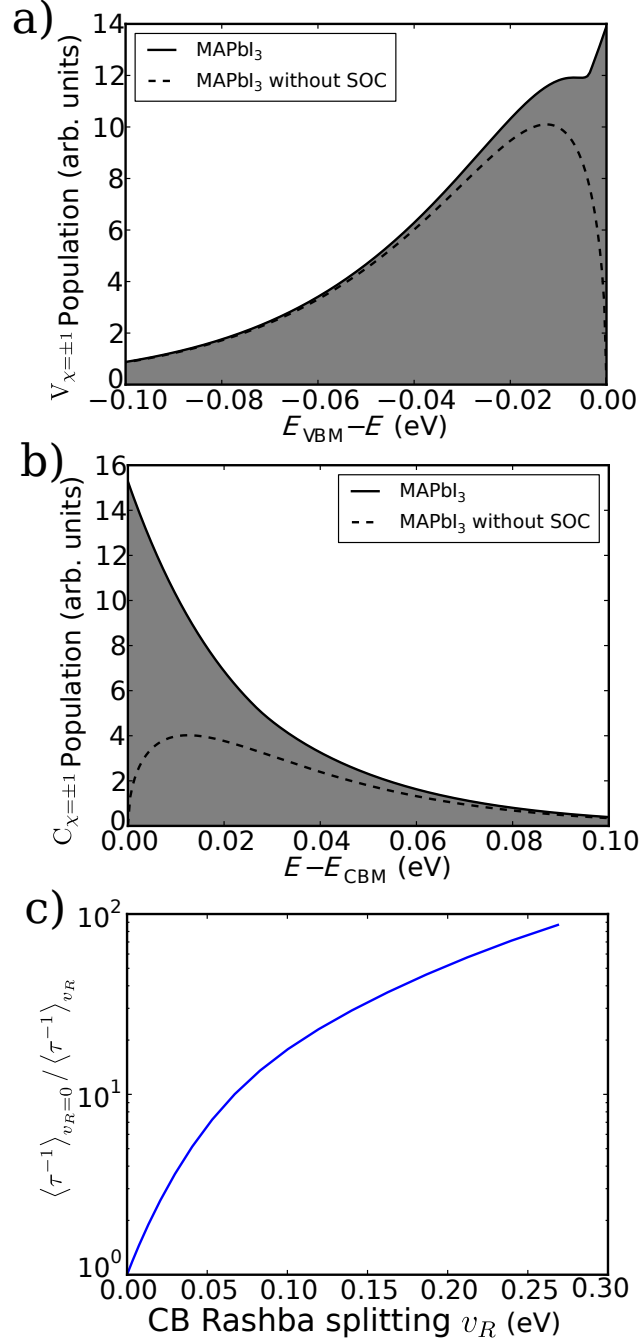


Figure 3: a) Population of carriers at $T=298$ K, calculated from the Fermi-Dirac distribution, for a) the top valence band and b) the bottom conduction band of MAPbI₃. Shown in dashed lines are the population of carriers in a model material with the same band masses as MAPbI₃, but with vanishing Rashba splitting. c) Unitless lifetime enhancement factor, as defined in the text, as a function of the conduction band Rashba splitting energy.

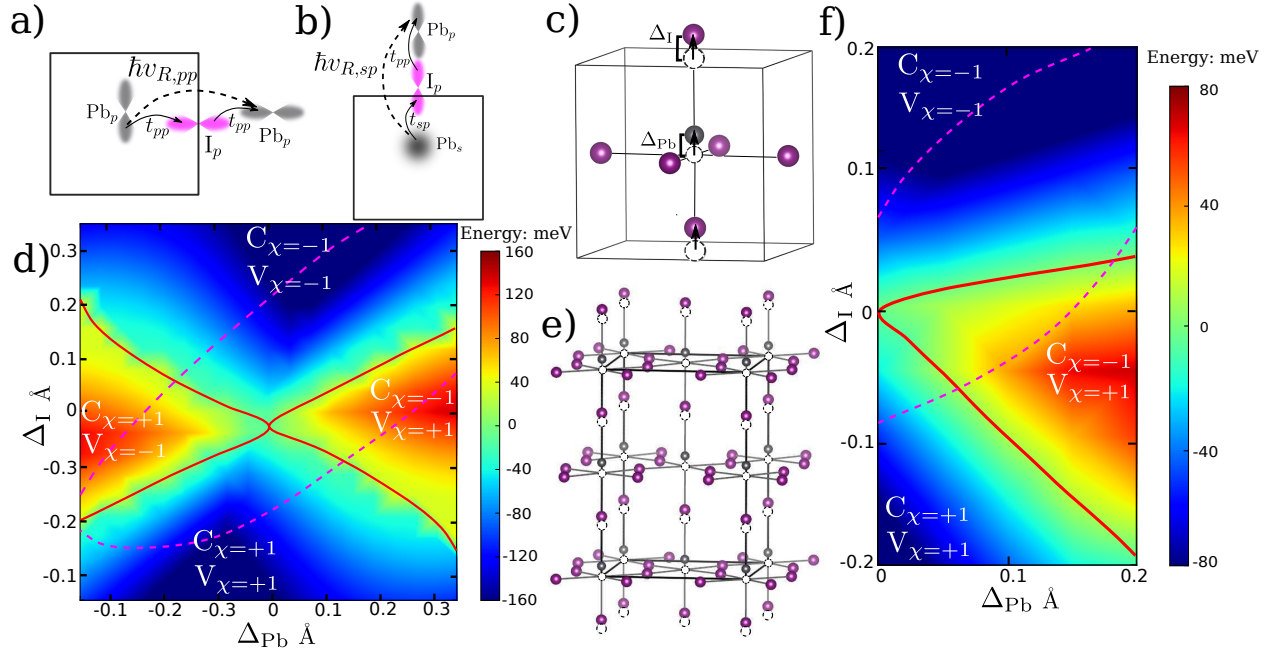


Figure 4: a) and b) Hopping schemes illustrate the effective electric field $\hbar v_{R,sp}$ and $\hbar v_{R,pp}$ created by vertical hopping and horizontal hopping respectively for a range of Pb and I displacements. These two factors caused by different Pb and I displacements controls spin textures of CBM and VBM differently, giving rise to different spin helicities. c) Schematic diagram showing Pb and I displacement in pseudocubic MAPbI₃. Pb: Silver. I: Indigo. Broken circles are original high-symmetry positions. Molecules are not shown here. d) Phase diagram of splitting energy and spin texture for structures with different Pb and apical I displacement in pseudocubic MAPbI₃ calculated from DFT. The color is the minimum value between the averaged splitting energy of two Rashba conduction bands and two valence bands (see Methods). The spin texture phase boundaries are indicated by the solid red lines. When the structure transforms from a favorable spin texture region to an unfavorable spin texture region, the two Rashba valence bands or conduction bands exchange, creating negative splitting energy. The dashed lines indicate the areas with energy cost less than 25 meV (under room temperature fluctuation) to distort Pb and I. e) Schematic diagram showing Pb and I displacement in tetragonal MAPbI₃. f) Similar to d, phase diagram of splitting energy and spin texture for structures with different Pb and apical I displacement in tetragonal MAPbI₃ calculated from DFT.